Surface phase diagram and stability of (001) and (111) $LiMn_2O_4$ spinel oxides

Soo Kim, Muratahan Aykol, and C. Wolverton*

Department of Materials Science and Engineering, Northwestern University, 2220 Campus Drive, Evanston, Illinois 60208, USA

(Received 30 April 2015; revised manuscript received 15 July 2015; published 10 September 2015)

The (001) and (111) surface structures of the $LiMn_2O_4$ (LMO) spinel are examined using density functional theory (DFT) calculations within the generalized gradient approximation (GGA) + U approach. In order to clarify discrepancies in the literature for previous DFT calculations of these surfaces, we first carefully study the effects of surface termination/reconstruction, slab construction, and relaxation schemes, as well as magnetic ordering and U values for Mn on the calculated surface energies of LMO. We explain these discrepancies and show that the relaxation scheme and surface reconstruction play the key role in determining the relative stability of (001) and (111) surfaces. We have further analyzed the thermodynamic stability of LMO surfaces as a function of oxygen and lithium chemical potentials. We have found that the ratio of (001) to (111) surface energies is ∼1.09 up to the oxygen chemical potential corresponding to ∼800 K. This ratio favors the formation of truncated-octahedron shaped LMO particles dominated by Li-terminated reconstructed (111) facets with no surface Mn, which can help suppress Mn dissolution. Higher temperatures or closed systems (with no exchange of material with surroundings) favor the formation of (001) dominated particles. The observation of a wide spectrum of polyhedral shapes between (001)- and (111)-dominated LMO particles in experiments can be explained by the narrow range of surface energies and their sensitivity to synthesis conditions.

DOI: 10.1103/PhysRevB.92.115411 PACS number(s): 68.35.B−, 68.47.Gh, 82.47.Aa, 81.30.Bx

I. INTRODUCTION

The spinel $LiMn_2O_4$ (LMO) has been investigated as a promising cathode candidate for Li-ion batteries because of its low cost, high voltage, and fast Li^+ diffusivity [1–14]. However, there are several drawbacks of LMO including a severe capacity fade during cycling due to a Jahn-Teller (JT) distortion in the oxide material, as well as dissolution of Mn in the electrolyte [1–14]. Since the dissolution can initiate from the surfaces of LMO particles, a complete understanding of the surface structure and stability is the key to suppress the Mn loss and to overcome the current limitations of the spinel LMO as a Li-ion battery cathode [2–4,11,12].

The electrochemical performance of batteries with LMO cathodes depends on multiple factors (e.g., phase transformation, particle size, raw materials, etc.), and in particular, the morphology of the LMO particles obtained with different synthesis conditions can lead to diverse electrochemical properties [5–7]. For example, Kim *et al.* demonstrated that the octahedron-shaped LMO cathode particles dominated by (111) surfaces exhibit a superior capacity retention compared to the platelet-shaped LMO dominated by (001) surface [7]. These findings suggest that the (111) LMO surface is more resistant to Mn dissolution, while other surfaces such as (001) are more likely to be more prone to it.

Density functional theory (DFT) calculations have a growing impact on battery materials research where they can describe material properties such as phase stabilities and diagrams, intercalation voltages, and surface energies of lithium-ion battery electrodes [2–4,11–23]. The LMO surface structure was not investigated until very recent years using DFT [2], and there are notable discrepancies in the reported LMO surface energies [2–4]. For instance, the reported energies for the same (001) Li-terminated surface vary from 0.26 to 0.96 J/m^2 [2–4]. There is also no clear consensus for the lowest energy crystallographic surface orientation. The Li-terminated (001) surface was suggested to have the lowest energy among the Li- and Mn/O-terminated (001), Mn/O- and Li/Mn/O-terminated (110), and O-, Li/Mn-, and, Li/Mn/O-terminated (111) surfaces studied in Refs. [2] and [3]. More recently, the Li-terminated (111) surface reconstructed by swapping surface Mn atoms with subsurface Li atoms (forming a partial inverse spinel arrangement [14,24,25]) was proposed to be the most stable surface among all the Li- and Mn/O-terminated (001), Mn/O- and Li/Mn/O-terminated (110), and Li/Mn/O- and reconstructed Li-terminated (111) surfaces in Ref. [4]. This reconstructed (111) surface has no Mn atoms near the surface, and therefore is consistent with the better capacity retention observed for the octahedral-shaped LMO particles dominated by (111) surfaces [7]. Furthermore, this (111) reconstructed surface [4] was recently incorporated to examine the decomposition reaction of ethylene carbonate on the (111) surface [11] and to calculate the redox potentials of removing Li from surface facets [12].

Depending on the ratio of (001) and (111) calculated surface energies [2–4], the Wulff shape of the LMO particles can vary from truncated-cube to cubo-octahedron to truncated-octahedron. Such a wide spectrum of LMO particle shapes have actually been observed in the experiments [7–10]. Synthesis of oxide particles such as LMO and the formation of surfaces during heat treatment often take place under conditions where material can be exchanged with the environment (e.g., heat treatment in air) and therefore morphologies dominated by (001) or (111) are all accessible by fine tuning of synthesis conditions (e.g., temperature, reaction time, precursor, and surfactant) [7]. It is not straightforward to extract relative surface energies from the experimentally synthesized particle shapes. Thus, there is neither experimental nor a computational agreement on the relative stabilities of (001) and (111) surfaces of LMO [2–4,7–10].

To reveal the mechanisms underlying Mn dissolution from LMO, it is critical to revisit the (001) and (111) calculated

*Corresponding author: c-wolverton@northwestern.edu

surface energies of LMO. In this work, we first examine both numerical and physical factors in DFT studies of LMO surfaces in an effort to explain the discrepancies of calculations in previous literature [2–4]. Specifically, we explore surface termination and reconstruction, supercell size and slab thickness, relaxation schemes, electronic and magnetic parameters, and subsequent convergence issues that can lead to conflicting surface energies for LMO. Carefully considering the effects of all these factors, we are able to provide accurate DFT energies for the (001) and (111) surfaces of LMO. We show that relaxation of all atomic positions with symmetry-broken DFT calculations is the most robust scheme to fully capture the local variations of Mn-O and Li-O polyhedral clusters from the surface of the slab to the bulk, and to eventually obtain converged DFT surface energies. When reference chemical potentials are acquired from the bulk Li-Mn-O phase diagram (i.e., a thermodynamic system closed to exchange of material with surroundings), our DFT calculations indicate that the (001) surface is only $\sim 0.05\,J/m^2$ more stable than the (111) surface with a (001) to (111) surface energy ratio of ~ 0.94. Under conditions open to exchange of material with the environment, i.e., heat treatment in presence of the O_2 gas, and Li chemical potentials where LMO is stable, we find that the (001) to (111) surface ratio is ~ 1.09 and does not vary up to ~ 800 K. The ratio starts to decrease and the (001) surface becomes more dominant at $\geqslant 800$ K. The fact that these two crystallographic facets are very close in energy (and the surface energy ratio is close to unity) is in accord with the sensitivity of the relative amounts of such surfaces to synthesis conditions in experiments [7–10].

II. METHODOLOGY

A. First-principles calculations

All DFT calculations were carried out using the Vienna Ab-initio Simulation Package (VASP) with the projected augmented wave (PAW) potentials, and Perdew-Burke-Ernzerhof (PBE) formulation of the generalized gradient approximation (GGA) [26–28]. We use Dudarev's rotationally invariant DFT + U functional to treat the *3d* electrons of Mn ions [29]. U values of 4.5 and 5 eV were both tested to investigate a possible source of the disagreements in previous studies [2,4]. We use a cutoff energy of 550 eV for the plane-wave basis set in all calculations. We tested using approximate k-point meshes with 8000 and 28 000 k points per reciprocal atom, and found that the former density is sufficient to obtain accurate total energies for bulk LMO. Both ferromagnetic (FM) ordering [3] and different antiferromagnetic (AFM) orderings along the [110] direction [2,4] were examined for the bulk and surface LMO slab structures. Ouyang *et al.* [2] adopted alternating spin up and down along the [110] direction (↑↓↑↓) and Karim *et al.* [4] adopted the [↑↑↓↓] pattern along the [110] direction; thus, we evaluated both AFM patterns. We further tested turning the symmetry operations off in DFT calculations to allow symmetry lowering distortions and to evaluate it as another possible source of disagreement among previous studies [2–4]. An appropriate k-point mesh of $2 \times 2 \times 1$ or $3 \times 3 \times 1$ was adopted for surface calculations depending on the slab thickness. Gaussian smearing with a smearing width of 0.1 eV was used for the surface calculations. Upon calculating the phase and surface stability diagrams, we consider the most stable forms of bulk Mn, Li, Li_2O, Li_2O_2, MnO, Mn_3O_4, Mn_2O_3, MnO_2, $LiMnO_2$, and Li_2MnO_3 in addition to $LiMn_2O_4$ in the Li-Mn-O chemical space in the Open Quantum Materials Database (OQMD) [22,30,31], and recalculate them here at a cutoff energy of 550 eV to preserve consistency with the rest of our calculations.

B. Surface slab calculations

For every planar termination we considered in this work, i.e., (001) and (111), we test three different approaches to construct the surfaces. These include building (i) a stoichiometric slab with asymmetric (i.e., nonequivalent) surfaces on either side of the slab (T1), (ii) a stoichiometric slab with symmetrically equivalent surfaces (T2), and (iii) an off-stoichiometric slab with identical terminations on each

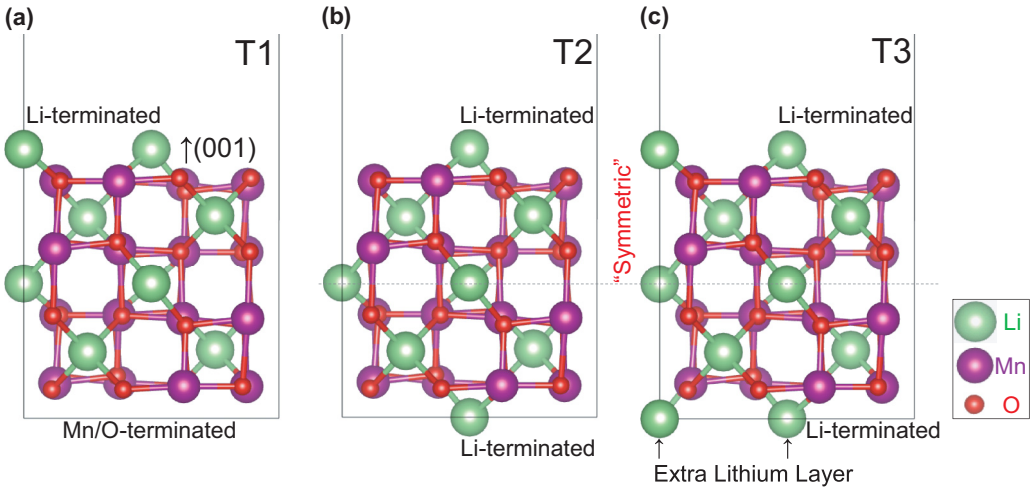

FIG. 1. (Color online) The atomic structures of the spinel LMO (001) surfaces: (a) T1: asymmetric Li- and Mn/O-terminated $Li_8Mn_{16}O_{32}$ surface (eight layers); (b) T2: symmetric Li-terminated $Li_8Mn_{16}O_{32}$ surface (a surface Li from the top surface was moved to the bottom surface; nine layers); (c) T3: symmetric Li-terminated off-stoichiometric $Li_{10}Mn_{16}O_{32}$ surface (nine layers). The green, purple, and red circles represent Li, Mn, and O atoms, respectively.

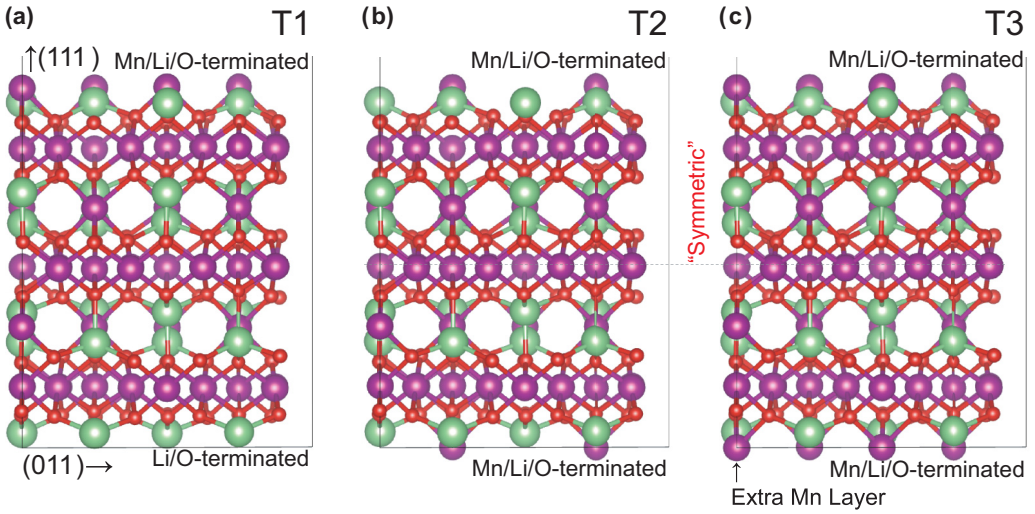

FIG. 2. (Color online) The atomic structures of the spinel LMO (111) surfaces: (a) T1: asymmetric Mn/Li/O- and Li/O-terminated $Li_{24}Mn_{48}O_{96}$ surface (18 layers); (b) T2: symmetric Mn/Li/O-terminated $Li_{24}Mn_{48}O_{96}$ surface (two surface Mn atoms from the top surface were moved to the bottom surface; 19 layers); (c) T3: symmetric Mn/Li/O-terminated off-stoichiometric $Li_{24}Mn_{52}O_{96}$ surface (an extra layer of four Mn atoms was added to the bottom surface; 19 layers).

surface (T3), as shown in Fig. 1. The first approach (T1) involves simply cleaving the bulk crystal across the given plane perfectly, yielding two flat but chemically distinct surfaces on top and bottom faces of the slab. This T1-type of termination is displayed in Fig. 1(a), where the top surface is composed of Li atoms while the other surface exposes the Mn-O layer. This is a Tasker III–type construction which cannot be stable due to its net dipole [32]. The second approach (T2) involves symmetrizing and removing the polarity of the surfaces created in T1 by transferring half of the atoms from one surface across the slab to the other surface, as illustrated in Fig. 1(b). Both surfaces of the slab are identical in T2, but they are undercoordinated with respect to the simple cleaved termination of T1. Both T1- and T2-type surfaces preserve the stoichiometry of the slab, however, the generated slab either has different chemistries and net charges on each surface (T1), or steps with atoms having fewer neighbors than the perfectly cleaved surface, i.e., with more unsaturated bonds (T2). The third approach (T3) is to create surfaces with identical chemistries on each side of the slab by introducing off-stoichiometry, as illustrated in Fig. 1(c). Employing these three different approaches, we also create three (111) surface slabs with varying surface constructions as shown in Fig. 2.

Surface reconstruction can also play a major role as a mechanism to stabilize surfaces, where the chemical identity of atoms on lattice sites and their positions near the surface no longer follow the symmetry of the parent crystal lattice [3,4]. For the current LMO system, it has been proposed by Karim *et al.* [4] that (111) surfaces may be reconstructed by swapping the Mn atoms in the octahedral surface sites with the tetrahedral Li atoms in adjacent layers. For all types of (111) surfaces created using the three approaches, T1, T2, and T3 described above, we also consider such reconstructions of (111) surfaces as shown in Fig. 3 (T1R)

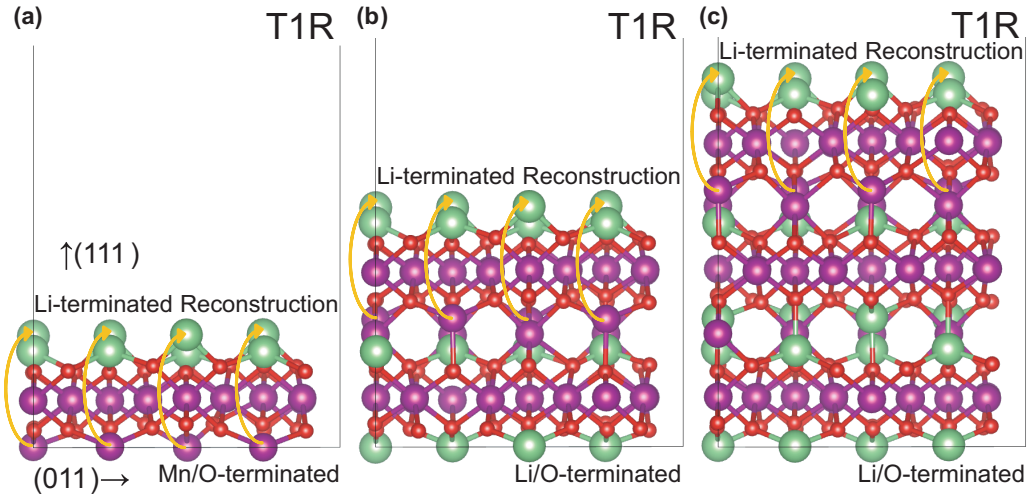

FIG. 3. (Color online) The atomic structures of the (111) LMO T1 surfaces with reconstruction (T1R) at the top surface: (a) $Li_8Mn_{16}O_{32}$ surface (six layers); (b) $Li_{16}Mn_{32}O_{64}$ surface (12 layers); (c) $Li_{24}Mn_{48}O_{96}$ surface (18 layers).

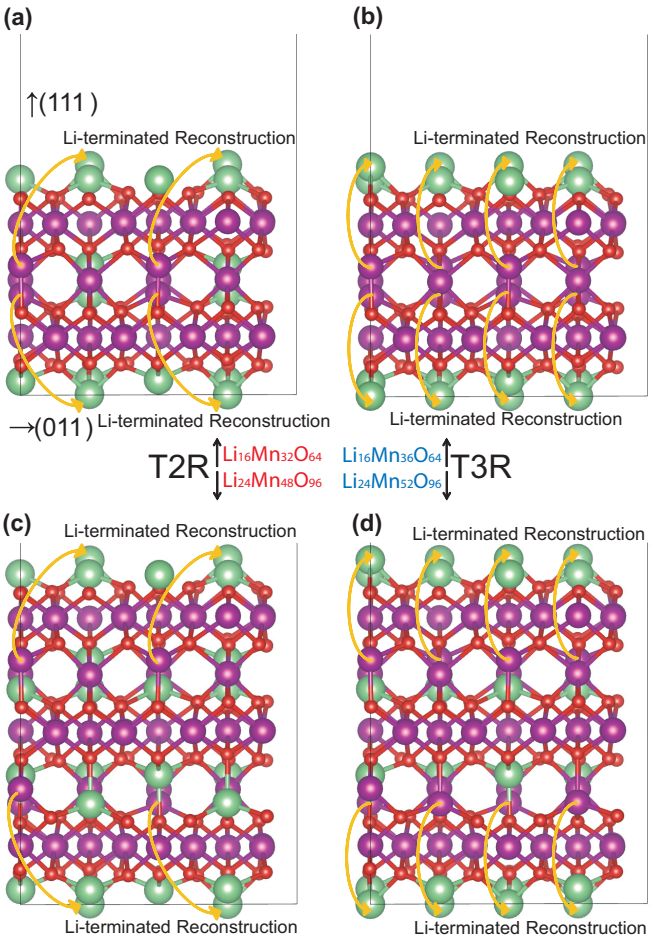

FIG. 4. (Color online) The atomic structures of the symmetrical spinel LMO (111) surfaces with reconstruction at the top and bottom surfaces (T2R and T3R): (a) $Li_{16}Mn_{32}O_{64}$ T2R surface (13 layers); (b) off-stoichiometric $Li_{16}Mn_{36}O_{64}$ T3R surface (13 layers); (c) $Li_{24}Mn_{48}O_{96}$ T2R surface (19 layers); (d) off-stoichiometric $Li_{24}Mn_{52}O_{96}$ T3R surface (19 layers).

and Fig. 4 (T2R and T3R). In this work, we have considered these T1-, T2-, and T3-type Li-terminated (001), T1-, T2-, and T3-type Mn/Li/O-terminated (111), and T1R-, T2R-, and T3R-type reconstructed (111) surfaces to find the lowest DFT surface energy facet for LMO. For all calculations, we used sufficient vacuum thicknesses (up to 24 Å) to ensure negligible interaction between the slab surfaces. We tested relaxing all internal and external degrees of freedom in slab calculations (with no change found in vacuum thickness), where LMO surface slabs would easily access the JT distortion.

In addition to the surface termination and reconstruction, we systematically investigate the effects of the slab thickness in conjunction with the slab relaxation schemes on the convergence of surface energies. In slab relaxation schemes, to use slabs as thin as possible, the positions of atoms are often fixed for a certain number of middle layers to maintain the bulklike behavior in the midsections, which will be discussed in Sec. III B 1. Thus, we have tested different schemes from relaxing only a few surface layers to relaxing all atoms in the LMO surface slabs in this work, as well as schemes with different constraints on the supercell volume (i.e., relaxations

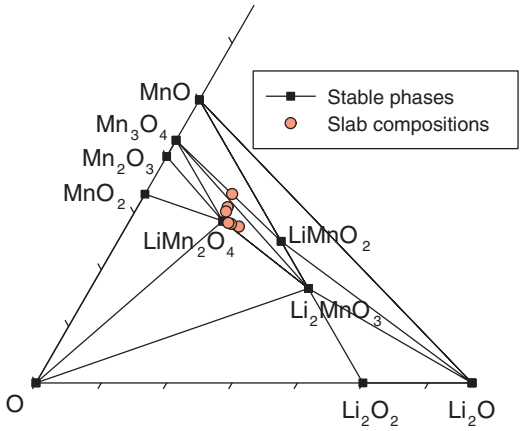

FIG. 5. (Color online) The calculated ground state ($T = 0$ K) phase diagram of the Li-Mn-O system near the O corner. Compositions of the off-stoichiometric T3-type slabs are also shown. Chemical potential of oxygen gas is obtained from Ref. [23], where it was fitted to experimental formation enthalpies of simple metal oxides extrapolated to $T = 0$ K.

where supercell vectors are fixed at the bulk lattice constants in plane of the surface, versus relaxations with no such constraints) for low surface energy LMO slabs. Furthermore, we test the effect of magnetic ordering and the U value for Mn atoms on the calculated surface energies of LMO.

C. Surface energies and thermodynamic stability diagrams

In general, the surface energy can be calculated with DFT as

$$\gamma = \frac{G_{\text{slab}} - \sum_i n_i \mu_i}{2A} \approx \frac{E^{DFT}_{\text{slab}} - \sum_i n_i \mu_i}{2A}, \qquad (1)$$

where G_{slab} is the free energy of the surface slab, n_i is the number of i atoms in the slab, μ_i is the reference chemical potential for the element i, and A is the surface area. For the surface cells that preserve the spinel stoichiometry (T1, T2, T1R, and T2R), $\sum_i n_i \mu_i$ is simply the bulk energy of LMO calculated with GGA + U multiplied by the number of formula units of LMO in the slab. However, for the nonstoichiometric slabs, the reference chemical potentials for Li, Mn, and O need to be defined. For closed systems (i.e., no atoms exchanged with the surroundings) at $T = 0$ K, we can obtain these reference chemical potentials (μ_i) from the mixture of ground-state phases present at the given off-stoichiometric composition in the phase diagram of Li-Mn-O system by solving equations $E^{DFT}_q = \sum_i n_{i,q} \mu_i$ defined for every stable phase q in the corresponding phase region ($n_{i,q}$ is the number of i atoms in phase q). The calculated Li-Mn-O (at $T = 0$ K) ground-state phase diagram near the O corner is shown in Fig. 5. This diagram contains the stable compounds (points), two-phase mixtures (tie lines), and three-phase equilibria (triangles) in Fig. 5. Compositions of T3 slabs mostly fall into the $LiMn_2O_4$-Mn_3O_4-Li_2MnO_3 region of the ternary phase diagram and are listed in Table I. Therefore, while the off-stoichiometry in real LMO particles with T3-type surfaces will certainly be much less than what we can achieve with thin slabs, the reference chemical potentials in the "closed

TABLE I. Compositions and reference phase mixtures for off-stoichiometric $Li_{1+x}Mn_2O_4$ and $LiMn_{2+x}O_4$ surface slabs obtained from DFT phase diagram in Fig. 5.

Chemical formula	Phase mixtures
$Li_{1+x}Mn_2O_4$-type slabs	
$Li_{10}Mn_{16}O_{32}$	$4.67\,LiMn_2O_4 + 2.67\,Li_2MnO_3 + 1.33\,Mn_3O_4$
$Li_{18}Mn_{32}O_{64}$	$12.67\,LiMn_2O_4 + 2.67\,Li_2MnO_3 + 1.33\,Mn_3O_4$
$Li_{26}Mn_{48}O_{96}$	$20.67\,LiMn_2O_4 + 2.67\,Li_2MnO_3 + 1.33\,Mn_3O_4$
$LiMn_{2+x}O_4$-type slabs	
$Li_8Mn_{20}O_{32}$	$8\,LiMnO_2 + 4\,Mn_3O_4$
$Li_{16}Mn_{36}O_{64}$	$5.33\,LiMn_2O_4 + 5.33\,Li_2MnO_3 + 6.67\,Mn_3O_4$
$Li_{24}Mn_{52}O_{96}$	$13.33\,LiMn_2O_4 + 5.33\,Li_2MnO_3 + 6.67\,Mn_3O_4$

system" will still stay the same as the composition of real samples will simply approach the LMO corner, i.e., always remain in this phase region.

In actuality, the synthesis conditions for LMO particles may deviate from such a "closed" thermodynamic system. For example, the system can be open to exchange of material and react with O_2 gas or a Li source. Therefore, the chemical potentials can be controlled externally by the synthesis conditions [33] and are not necessarily fixed by other stable phases near LMO in the ternary phase diagram. Thus, we should further analyze the stability of LMO and its surfaces as a function of chemical potentials. Thermodynamic stability condition for bulk LMO can be written as

$$G_{\mathrm{LiMn2O4}} = \mu_{\mathrm{Li}} + 2\mu_{\mathrm{Mn}} + 4\mu_{\mathrm{O}} \tag{2}$$

and for any other phase q in the Li-Mn-O system, the condition

$$G_q > \sum_i n_{i,q}\mu_i = n_{\mathrm{Li},q}\mu_{\mathrm{Li}} + n_{\mathrm{Mn},q}\mu_{\mathrm{Mn}} + n_{\mathrm{O},q}\mu_{\mathrm{O}} \tag{3}$$

ensures that phase q does not have a thermodynamic tendency to precipitate, where the free energy of phases are denoted as G. In conjunction with the stability of bulk LMO, surface free energies can be calculated as in Eq. (1) as a function of chemical potentials. Since the surface must be in equilibrium with the bulk, only two of the chemical potentials in Eq. (1) are independent because the third potential is always constrained by Eq. (2). The same is true in Eq. (3) for the precipitation of phases other than LMO, where only two of the chemical potentials can be varied independently. We choose the oxygen and lithium chemical potentials, i.e., μ_{O} and μ_{Li} as our independent chemical potentials and calculate the surface and bulk LMO stability diagrams.

Except for the O_2 gas, all phases considered in the Li-Mn-O system are solids, so we assume temperature and pV contributions to their free energies are negligible compared to the O_2 gas, and their free energies $G(T,p)$ can be approximated as their GGA or GGA + U total energies, $E^{GGA(+U)}$. Here, $E^{GGA(+U)}$ refers to the GGA + U total energy for all Mn containing oxides and GGA energy for other solid phases. To overcome the incompatibility of the GGA calculation of elemental Mn and GGA + U calculations of Mn oxides, the chemical potential of elemental Mn can be written as $\mu^{el.}_{\mathrm{Mn}} = \mu^{GGA}_{\mathrm{Mn}} + \mu^{\mathrm{corr}}_{\mathrm{Mn}}$, where we find the correction factor $\mu^{\mathrm{corr}}_{\mathrm{Mn}}$ to be 2.097 eV by averaging the correction factors calculated for MnO, Mn_2O_3, and MnO_2 at $U_{\mathrm{Mn}} = 5$ eV as described in Refs. [23] and [34].

The chemical potential of gaseous oxygen at finite temperature and pressure can be defined as $\mu_{\mathrm{O}}(T,p) = \frac{1}{2}[\mu^{\circ}_{O2}(T) + RT\ln p_{O2}]$, where the standard free energy of O_2 gas is $\mu^{\circ}_{O2}(T) = \mu^{0K}_{O2} + \Delta g^{\circ}_{O2}(T)$. Here, the free energy of O_2 at $T = 0$ K is μ^{0K}_{O2}, which we approximate as $\mu^{GGA-fit}_{O2}$; i.e., the chemical potential of O_2 gas fitted to 0 K experimental formation enthalpy data of simple metal compounds as reported in Ref. [23]. Since it was fitted to experimental data, this term includes the zero-point energy of the O_2 molecule as well. The term $\Delta g^{0}_{O2}(T)$ is the change in standard free energy of O_2 gas from 0 K to T under standard pressure of 1 atm, and is taken from the experimental data reported in JANAF thermochemical tables [35]. The chemical potential of oxygen can be given with respect to μ^{0K}_{O2} as $\Delta\mu_{\mathrm{O}} = \mu_{\mathrm{O}}(T,p) - \frac{1}{2}\mu^{0K}_{O2} \approx \mu_{\mathrm{O}}(T,p) - \frac{1}{2}\mu^{GGA-fit}_{O2}$. Similarly, we give the Li chemical potential in stability diagrams with respect to bulk Li, i.e., $\Delta\mu_{\mathrm{Li}} = \mu_{\mathrm{Li}} - \mu^{bcc}_{\mathrm{Li}}$, where μ^{bcc}_{Li} is the GGA total energy of elemental Li in the body-centered-cubic structure.

Furthermore, the Wulff shapes were generated using the Wulffmaker [36]. VESTA was used to create and visualize surfaces [37].

III. RESULTS AND DISCUSSION

A. Bulk LMO

The relaxation of bulk LMO with a FM structure and symmetry operations preserved yields lattice constants of $a = b = c = 8.46$ Å with cubic symmetry ($\alpha = \beta = \gamma = 90^{\circ}$), consistent with the literature [4]. The [110]-type AFM ordering with a [↑↑↓↓] spin configuration is found to be slightly more stable (by 4 meV/atom) than the [↑↓↑↓] configuration. Both AFM spin configurations produce a JT distortion along the z direction ($a = 8.25$, $b = 8.28$, $c = 8.77$ Å, with $\alpha \approx \beta \approx \gamma \approx 90^{\circ}$). In fact, we find that when the symmetry is turned off, a JT distortion similar to the AFM calculations can be captured even with FM ordering ($a = 8.26$, $b = 8.29$, $c = 8.78$ Å; $\alpha = 90.30$, $\beta = 89.82$, $\gamma = 90.45^{\circ}$). The symmetry-broken FM relaxation (i) captures the JT distortion of Mn^{3+}, (ii) is almost degenerate with the AFM [↑↑↓↓] ordering, and (iii) is 40 meV/atom more stable than the cubic FM ordering. We also find that slight variations in U values for Mn as used in previous studies [2–4,38] (4.5 or 5 eV) do not have a considerable effect on the properties discussed above.

B. Surface energies of LMO

1. The (001) surface

The (001) surface energies reported for LMO in the literature vary between 0.26 and 0.96 J/m^2, despite all being calculated with DFT using GGA + U functionals [2–4]. Ouyang *et al.* [2] used GGA + U ($U = 4.5$ eV) and ultrasoft pseudopotentials [39]. In Refs. [3] and [4], GGA + U calculations were carried out using the PW91 and PBE exchange-correlation functionals, respectively [26–28,40]. Benedek *et al.* [3] used the FM ordering with $U = 4.84$ eV, while Karim *et al.* [4] used the AFM ordering with $U = 5$ eV. We found that using

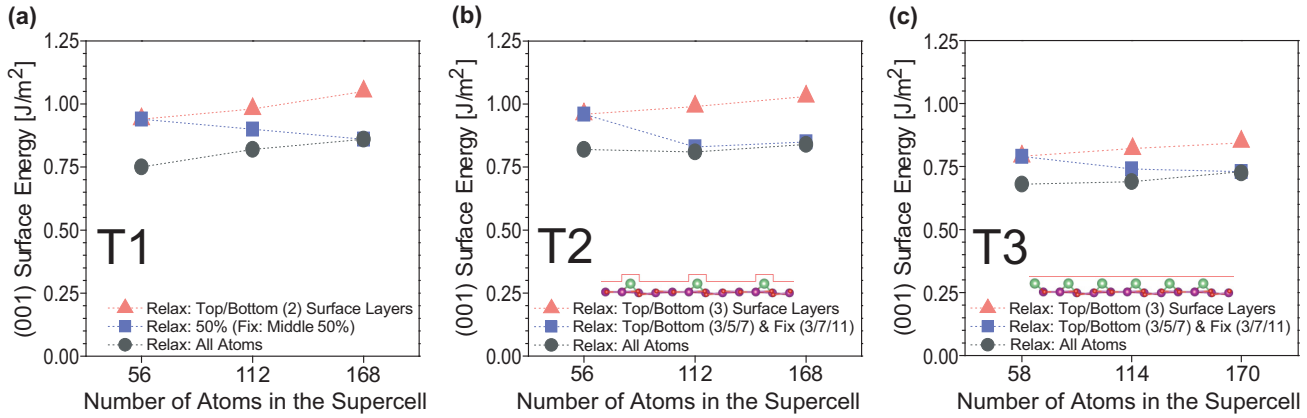

FIG. 6. (Color online) Calculated DFT (001) surface energies with increasing slab thicknesses: (a) Li- and Mn/O-terminated T1 surface, (b) Li-terminated T2 surface, and (c) Li-terminated T3 surface. T2-type surface is undercoordinated with respect to the surface shown in T3. Different relaxation schemes were performed from relaxing few surface layers to relaxing the entire slab. For example, T2-type 112 atoms LMO in (b), both top and bottom layers (five layers each) were relaxed, while the bulk regions (seven layers) were fixed [blue square (112 atoms)]. T1-(001) surfaces have 8, 16, and 24 layers with increasing number of atoms in the supercell, respectively. T2- and T3-(001) surfaces always have one extra layer compared with T1-(001) surfaces.

slightly different U values (4.5 or 5 eV), assigning AFM or FM ordering with no symmetrization, or changing the amount of vacuum (8 or 16 Å) does not have a considerable effect on the calculated (001) surface energies, i.e., they converge within 0.01 J/m^2. Therefore, we suggest that these factors alone cannot explain the disagreements among the reports in literature [2–4]. In addition, we confirmed that the Mn/O-terminated (001) surface has a higher surface energy than the Li-terminated (001) surface, as already found in previous works [2–4].

We show the calculated energies of T1-, T2-, and T3-type Li-terminated (001) surfaces as a function of slab thickness and relaxation schemes in Fig. 6. For the stoichiometric LMO slabs (T1- and T2-type), the bulk energy of LMO can be subtracted to calculate the surface energies. On the other hand, T3-type slab surface energies can vary as a function of chemical potentials of constituent elements in Eq. (1). While investigating the surface energy convergence, the chemical potentials for Li-terminated T3 slabs in Fig. 6(c) are referenced to the phase mixtures in Table I acquired from the calculated ground-state phase diagram in Fig. 5.

In Fig. 6, we find that an eight-layer-thick slab or relaxing only the top two layers of this eight-layer slab similar to Ref. [4] are both inadequate to obtain well-converged (001) surface energies, regardless of the type of surface termination. In fact, relaxing the atomic positions in the top two layers on each side of the slab misleadingly converges to around 0.1–0.2 J/m^2 higher energies than a fully converged relaxation scheme. The two other schemes, i.e., relaxing 50% of the slab (for odd number of layers, the ratio deviates from the 50%) and relaxing the entire slab, converge to almost the same surface energy for all different surface constructions as shown in Figs. 6(a)–6(c). The T1-type Li- and Mn/O-terminated (001) surface, T2-type Li-terminated (001) surface energies converge to 0.86 and 0.84 J/m^2, respectively. The T3-type Li-terminated (001) surface converges to 0.72 J/m^2 with respect the chemical potentials from the ternary phase diagram in Fig. 5. While this T3-(001) surface turns out to be the most stable one with respect to the set of chemical potentials acquired from the phase diagram in Fig. 5, its energy will vary as a function of the environmental conditions (i.e., chemical potentials), which we will discuss in Sec. III C. Last, in all panels of Fig. 6, it is clearly seen that the fastest converging scheme is the one where all atoms of the slab are relaxed, predicting surface energies closest to the converged values even in the smallest supercell with 56 atoms.

2. The (111) surface (unreconstructed)

The (111) surface calculations shown in Fig. 7 also follow the same procedures we used in the (001) surface calculation in Fig. 6. However, for (111) surface calculations, we relaxed all atoms in the supercells, since we have already showed in Fig. 6 that this method gives the most consistently converged surface energies. For the thinnest slab in Fig. 7(a), we find the T2-type (111) $Li_8Mn_{16}O_{32}$ surface energy to be 1.21 J/m^2, which is very close to the 1.18 J/m^2 reported for the same surface by Karim *et al.* [4]. However, as we increase the slab thickness, we find that T1- and T2-type (111) surfaces converge to a smaller energy of ~1.08 J/m^2 as shown in Fig. 7(a). Thus, the local structural distortions induced in subsurface layers by the presence of the LMO surface could not vanish in the thinnest slab model. In general for the LMO system, when the slab thickness is sufficiently large and stoichiometry of LMO is preserved, the surface energy obtained from the asymmetric surface (T1) is very similar to the symmetrized surface (T2) energy both for (001) and (111) [see Figs. 6 and 7].

For the T3-type (111) surface in Fig. 2(c), there are four additional Mn atoms added to the bottom surface shown in Fig. 2(a). Therefore, as explained in Sec. II B, energies of these T3-type surfaces will be a function of chemical potentials of elements. For convergence tests, we again use the reference phase mixtures from the ground-state phase diagram in Fig. 5 for such $LiMn_{2+x}O_4$ slabs as listed in Table I. The composition of the thinnest T3 slab $Li_8Mn_{20}O_{32}$ falls on the overlithiated spinel $LiMnO_2$ (i.e., $Li_2Mn_2O_4$) and Mn_3O_4 tie line in Fig. 5 and therefore the corresponding

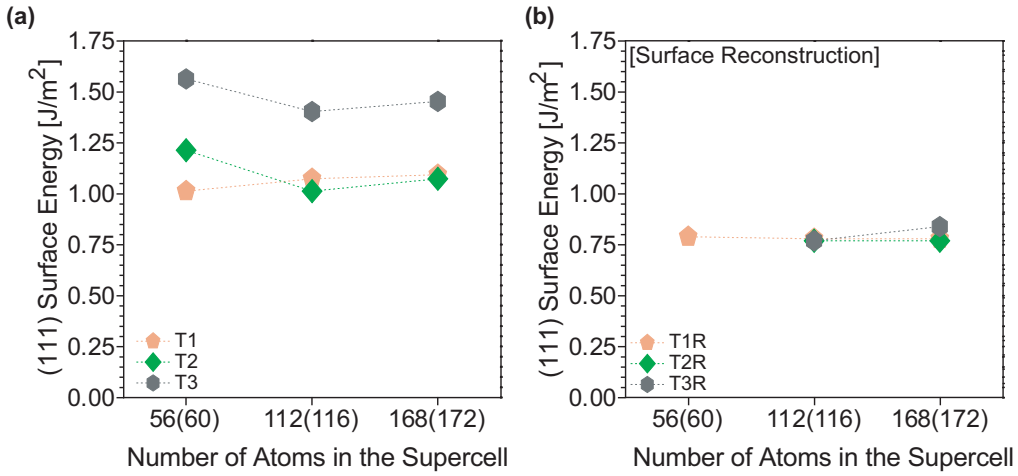

FIG. 7. (Color online) Calculated DFT surface energies with increasing slab thicknesses: (a) unconstructed (111) surface energies for T1, T2, and T3 and (b) reconstructed-(111) surface energies (T1R, T2R, and T3R). The nonstoichiometric T3- and T3R-type surfaces have additional atoms in the supercell compared with the stoichiometric surface slabs, as shown in the parentheses.

ground-state phase mixture does not contain LMO. The LMO spinel does not become a major component of the phase mixture (>50%) until a thicker slab of 24 formula units is used, and the corresponding compositions all fall into the $LiMn_2O_4$-Mn_3O_4-Li_2MnO_3 region in the phase diagram in Fig. 5.

3. *The reconstructed-(111) surface*

The (111) facet reconstructions have been found to be stable in the inverse spinel arrangement [14,24,25], and we apply the reconstruction described by Karim *et al.* [4] to the (111) surfaces as shown in Figs. 3 and 4. The respective surface energies are plotted in Fig. 7(b) as a function of slab thickness. For several slabs, reconstruction could not be performed. The T1R-, T2R-, and (T3R)-type $Li_8Mn_{16(20)}O_{32}$ slabs are too thin to carry out the reconstruction at both terminated surfaces. For the T1R $Li_8Mn_{16}O_{32}$ slab, the reconstruction was performed only at the top surface as shown in Fig. 3(a). Also, the T1R slabs in Figs. 3(b) and 3(c) have the Li/O termination at the bottom surface, where Li/Mn swapping cannot be incorporated. For the reconstruction of the T2R surfaces in Figs. 4(a) and 4(c), four pairs of the Li/Mn atoms were exchanged. For the T3R surfaces, eight pairs of the atom swapping were carried out as shown in Figs. 4(b) and 4(d). A relaxation scheme with only the top two and the bottoms two layers relaxed as described in Ref. [4] may not provide accurate energies in this case, since the local environment of Li that replaces Mn in the bulk after reconstruction needs to be relaxed as well. Comparing Figs. 7(a) to 7(b), we see that reconstruction notably lowers the (111) surface energies. The energies of the T1R- and T2R-type (111) converge to 0.78 and 0.77 J/m^2, respectively. These reconstructed (111) surface energies are close to the corresponding (001)

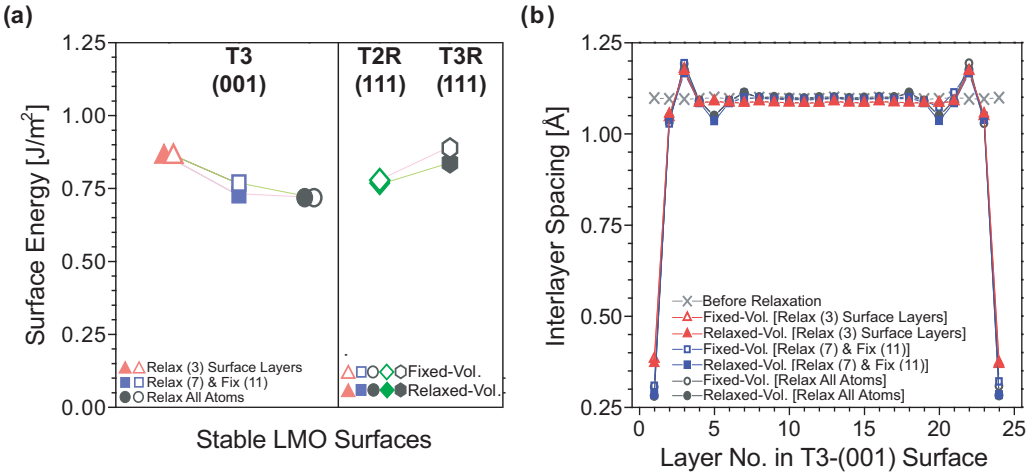

FIG. 8. (Color online) (a) LMO surface energies obtained from calculations with in-plane supercell vectors constrained to bulk lattice parameters (i.e., fixed-volume supercell calculation) for T3-(001) (170 atoms), T2R-(111) (168 atoms), and T3R-(111) (172 atoms) compared to the corresponding surface energies obtained by calculations with no such constraints (i.e., relaxed-volume supercell calculations). (b) Interlayer spacing before/after the relaxations with different schemes for T3-(001) LMO surface (170 atoms). The vertical axis indicates the interlayer spacing between the layer number (n) and the next adjacent layer ($n + 1$) from the horizontal axis.

surface energies. Because the (111) reconstructed surface energy is much lower than the unconstructed (111) surface energy, the experimentally observed (111) surface is consistent with the Li-terminated (111) surface stabilized by reconstruction. The energy of the T3R-type (111) surface converges to $0.84\,J/m^2$ with respect to the chemical potentials acquired from the ternary phase diagram, but its energy will vary with chemical potentials due to the nonstoichiometry of T3 terminations.

4. *Constrained and unconstrained supercell volume calculations*

For low surface energy LMO slabs T3-type (001) and T2R- and T3-type (111) surfaces, we compare the surface energies obtained from calculations with fully constrained supercell vectors (i.e., fixed-volume supercell calculation where the slabs are constrained to the bulk lattice parameters in plane of the surface) to relaxed-volume supercell calculation where there are no such constraints in Fig. 8(a). Karim *et al.* [4] previously showed that when the supercell volumes are allowed to relax, the obtained relative stabilities of surfaces and surface energies for different facets remain similar to the fixed supercell volume calculations. Confirming the results of Karim *et al.* [4], we also find that the differences in surface energies obtained with the relaxed- and fixed-volume calculations are small (all less than $0.05\,J/m^2$) as shown in Fig. 8(a). In Fig. 8(b), we further show that the interlayer spacing profiles in the direction perpendicular to the surface in the T3-type (001) slab obtained with different relaxation schemes are very similar. In the midsections of the slabs, the interlayer spacings remain close to the bulk values, and therefore a bulklike behavior is maintained in all fixed- or relaxed-volume supercell calculations. The change in lattice parameters parallel to the surface are also relatively small, i.e., less than 1% when supercell vectors are allowed to relax in the directions parallel to the surface.

C. Stability diagram for bulk LMO and LMO surfaces

Having systematically calculated the surface slab energies of LMO, we now construct the thermodynamic stability diagram in Fig. 9 to reveal how stability of bulk LMO and LMO surfaces correlate as a function of oxygen and lithium chemical potentials. We find that bulk LMO is stable in a chemical potential range bounded by the precipitation of Mn_2O_3, MnO_2, and Li_2MnO_3, where the precipitation line for Mn_3O_4 also approaches the stability region of LMO at high temperatures. These compounds and the associated temperature ranges for the stability of LMO agree very well with most of the experimental studies on the synthesis of LMO [7–10,41–43].

There are three main stability areas for surfaces in Fig. 9: T3-(001), T2R-(111), and T3R-(111). We find that the stability window of bulk LMO overlaps mostly with the stability region of T2R-(111) and extends into the stability region of T3-(001). Therefore, (111) and (001) dominated particles are both accessible upon synthesis for bulk LMO depending on the synthesis conditions. We observe in Fig. 9 that a lower temperature route is more likely to result in LMO particles with T2R-(111) dominated surface than a high temperature route. The T3R-type (111) particle surface is not accessible in

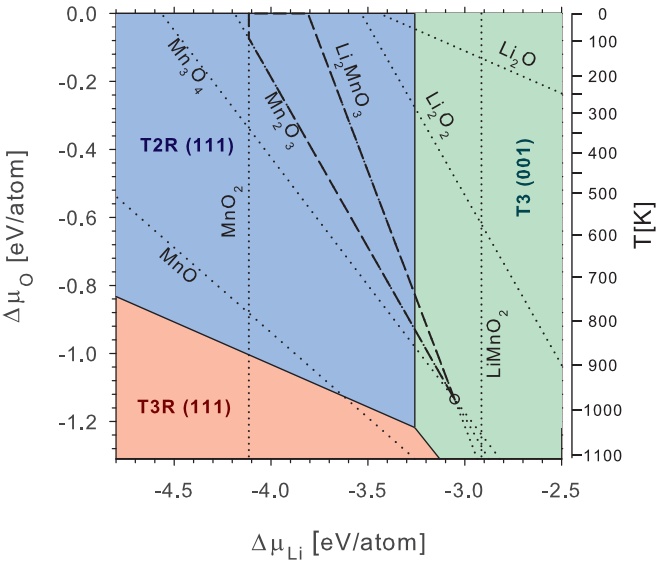

FIG. 9. (Color online) Thermodynamic stability diagram of bulk $LiMn_2O_4$ (LMO) and LMO surfaces as a function of oxygen and lithium chemical potentials. Solid lines separate the stability regions of different types of surfaces whereas dotted lines correspond to precipitation of the marked phases [Eq. (3)]. The dashed lines enclose the stability region of LMO. Temperature scale on the y axis corresponds to $p_{O2} = 0.2$ atm, and is based on the experimental free energy of O_2 gas as described in Sec. II. For comparison, the small circle shows $\Delta\mu_O$ and $\Delta\mu_{Li}$ corresponding to the $LiMn_2O_4$-Mn_3O_4-Li_2MnO_3 region of the ternary ground-state phase diagram in Fig. 5.

or near the stability window of bulk LMO; that is, it is less likely to form than its T2R-type analog during synthesis open to atmosphere. The T3-(001) surface is stable only at high temperatures and high Li chemical potentials when bulk LMO is synthesized in air.

While the particle shape for a given pair of oxygen and lithium chemical potentials will certainly be dominated by the most stable surface in Fig. 9, minimization of total surface energy in Wulff construction requires the energies of other surfaces as well. A variety of particle shapes between an octahedron of purely (111) facets and a cube with purely (001) facets can be obtained depending on the ratio of (001) and (111) surface energies. More stable (111) surfaces will yield structures such as the truncated octahedron, while increasing the stability of (001) surfaces will add more cubelike character to particles and alter the shapes to cubo-octahedron or truncated cubes. We compare the surface free energies as a function of lithium chemical potential at two different oxygen chemical potentials corresponding to 300 and 800 K at $p_{O2} = 0.2$ atm in Fig. 10. In the range of Li chemical potentials that stabilizes bulk LMO at 300 K in air, the T2R-(111) surface has the lowest energy, but the T2-(001) is only slightly higher in energy. Up to ~800 K, the stability regions of bulk LMO and of T2R-(111) overlap (Figs. 9 and 10), and the ratio of the energies of the most stable (001) and (111) surfaces remains fixed at ~1.09. Starting slightly below 800 K, the surface stability shifts from T2R-(111) to T3-(001) within the stability window of bulk LMO with increasing Li chemical potential as shown in Figs. 10 and 11 for 800 K. Therefore, from low temperatures to around 800 K and under synthesis conditions that favor

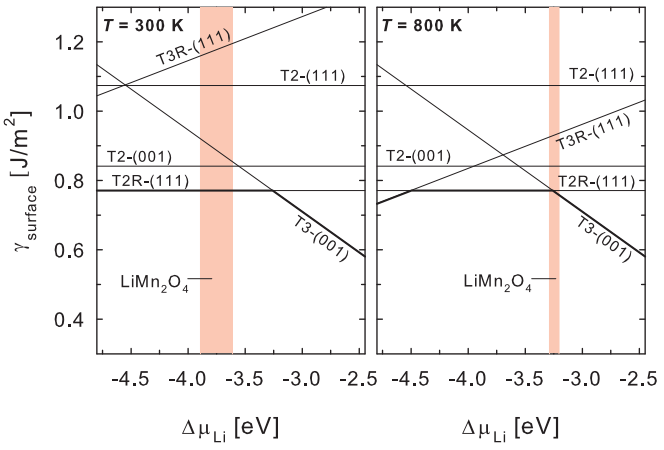

FIG. 10. (Color online) Surface energies of LMO as a function of Li chemical potential at O chemical potentials corresponding to $T = 300$ and 800 K (assuming an oxygen partial pressure p_{O2} of 0.2 atm). Bold lines represent the lowest surface energies as a function of Li chemical potential. Shaded regions show the stability range of bulk LMO.

stability of LMO without any precipitation of other phases, the equilibrium shape of the LMO particle is predicted to be a truncated octahedron with a (001) to (111) surface energy ratio of 1.09. At higher Li chemical potentials and temperatures, this ratio sharply decreases to form (001) dominated particles, as shown in Fig. 11.

The energies of (001) and (111) surfaces being very close agrees with the ease of tuning the surface ratios by varying synthesis conditions as shown by Kim *et al.* [7] If (111) surfaces are composed of Li-rich surface layers rather than the Mn-rich, the LMO spinel particles with (111) facets could be more resistant to the Mn dissolution, compared to the particles dominated by (001) or (110). Thus, we can speculate that in cases where experiments show a severe Mn dissolution of LMO cathode particles, these samples are likely to contain more (001) surfaces

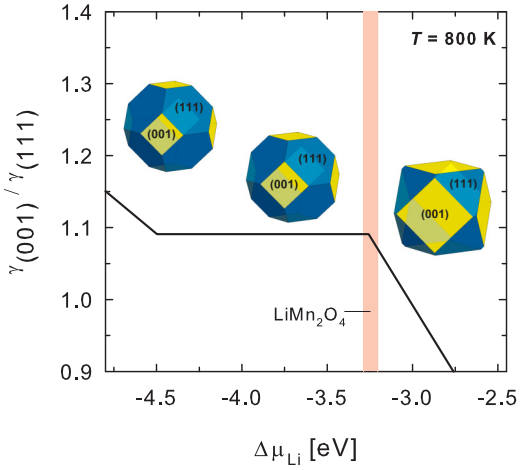

FIG. 11. (Color online) The (001) to (111) surface energy ratio and the corresponding representative LMO particle shapes as a function of Li chemical potential at an oxygen chemical potential corresponding to $T = 800$ K and p_{O2} of 0.2 atm. Shaded region shows the stability range of bulk LMO.

with the particle morphologies similar to Ref. [9]. Based on Figs. 9–11, we suggest that Li-excess environments and too high temperatures should be avoided upon synthesis to yield particles with less (001) character (i.e., surfaces more prone to Mn dissolution). In addition, higher synthesis/sintering temperatures lead to narrow chemical potential windows for the stability of LMO. Such narrow windows will increase the chances of LMO to decompose into other phases such as Mn_3O_4, Mn_2O_3, $LiMnO_2$, or Li_2MnO_3 as observed in several experiments [44–46], which will lead to poor electrochemical performance [44,45].

We should note that the above conclusions are for synthesis of LMO under equilibrium conditions that allow exchange of Li and O with surroundings. Synthesis conditions such as under vacuum or an inert gas with limited or no exchange of material with the surroundings may be represented more closely as a closed system with reference chemical potentials defined by the ternary phase diagram as discussed in Sec. III B. In that case, as shown in Figs. 6 and 7 (and also superimposed on Fig. 9 for comparison) the T3-(001) will be the most stable surface with an energy of 0.72 J/m^2 followed by the T2R-(111) with an energy of 0.77 J/m^2, and the corresponding (001) to (111) energy ratio of ~0.94 will lead to a truncated-cube-like particles.

IV. CONCLUSION

We have carefully analyzed different stoichiometric and nonstoichiometric surface models to calculate the (001) and (111) surface energies of LMO using GGA + U calculations. We find that the effect of LMO surfaces on the local geometry of subsurface layers is long ranged, and therefore the surface energies converge slowly with respect to the number of layers employed parallel to the surface planes in slab models. The slab relaxation schemes play a critical role in calculation of the surface energies, and relaxing all atoms in the slabs gave us the most consistent values.

Our calculations indicate that the (001) and (111) surface energies are very close and their relative ratio can be easily altered under varying experimental synthesis conditions, which explains the spectrum of cubelike to octahedronlike particle shapes obtained in experiments. Under synthesis conditions open to atmosphere and chemical potentials that stabilize LMO, the ratio of (001) to (111) surface energy is ~1.09 and the resulting LMO particles are predicted to be truncated-octahedron-like below ~800 K. Higher temperatures and high lithium chemical potentials should be avoided to obtain LMO particles dominated by reconstructed-(111) surfaces with no Mn atoms, which might mitigate the Mn dissolution. Synthesis conditions similar to a closed system (i.e., no exchange of material with the surroundings) are predicted to result in LMO particles with more (001) facets, i.e., more cubic character.

ACKNOWLEDGMENTS

S.K. was supported by Northwestern-Argonne Institute of Science and Engineering (NAISE). M.A. and C.W. were supported by The Dow Chemical Company. This research used resources of the National Energy Research Scientific Computing Center, a DOE Office of Science User Facility supported by the Office of Science of the U.S. Department

of Energy under Contract No. DE-AC02-05CH11231. The authors gratefully acknowledge fruitful discussions with Dr. J. R. Croy and Dr. M. M. Thackeray at Argonne National Laboratory. We also thank J.-K. Noh and Dr. B.-W. Cho at Korea Institute of Science and Technology and Z. Lu at Northwestern University for helpful discussions and advice.

[1] R. J. Gummow, A. de Kock, and M. M. Thackeray, Solid State Ionics **69**, 59 (1994).
[2] C. Y. Ouyang, X. M. Zeng, Ž. Šljivancanin, and A. Baldereschi, J. Chem. Phys. C **114**, 4756 (2010).
[3] R. Benedek and M. M. Thackeray, Phys. Rev. B **83**, 195439 (2011).
[4] A. Karim, S. Fosse, and K. A. Persson, Phys. Rev. B **87**, 075322 (2013).
[5] K. Matsuda and I. Taniguchi, J. Power Sources **132**, 156 (2004).
[6] I. Taniguchi, C. K. Kim, D. Song, and M. Wakihara, Solid State Ionics **146**, 239 (2002).
[7] J.-S. Kim, K. Kim, W. Cho, W. H. Shin, R. Kanno, and J. W. Choi, Nano Lett. **12**, 6358 (2012).
[8] T. Takada, H. Hayakawa, H. Enoki, E. Akiba, H. Slegr, I. Davidson, and J. Murray, J. Power Sources **81**, 505 (1999).
[9] H.-W. Chan, J.-G. Duh, S.-R. Sheen, S.-Y. Tsai, and C.-R. Lee, Surf. Coat. Technol. **200**, 1330 (2005).
[10] L. Yu, X. Qui, J. Xi, W. Zhu, and L. Chen, Electrochim. Acta **51**, 6406 (2006).
[11] N. Kumar, K. Leung, and D. J. Siegel, J. Electrochem. Soc. **161**, E3059 (2014).
[12] M. Nakayama, H. Taki, T. Nakamura, S. Tokuda, R. Jalem, and T. Kasuga, J. Phys. Chem. C **118**, 27245 (2014).
[13] A. Van der Ven, C. Marianetti, D. Morgan, and G. Ceder, Solid State Ionics **135**, 21 (2000).
[14] J. Bhattacharya and C. Wolverton, Phys. Chem. Chem. Phys. **15**, 6486 (2013).
[15] C. Wolverton and A. Zunger, Phys. Rev. Lett. **81**, 606 (1998).
[16] C. Wolverton and A. Zunger, J. Electrochem. Soc. **145**, 2424 (1998).
[17] A. Van der Ven and G. Ceder, Phys. Rev. B **59**, 742 (1999).
[18] J. Reed, G. Ceder, and A. Van der Ven, Electrochem. Solid State Lett. **4**, A78 (2001).
[19] D. Morgan, B. Wang, G. Ceder, and A. van de Walle, Phys. Rev. B **67**, 134404 (2003).
[20] M. Wagemaker, A. Van Der Ven, D. Morgan, G. Ceder, F. M. Mulder, and G. J. Kearley, Chem. Phys. **317**, 130 (2005).
[21] J. Hafner, C. Wolverton, and G. Ceder, MRS Bull. **31**, 659 (2006).
[22] S. Kirklin, B. Meredig, and C. Wolverton, Adv. Energy Mater. **3**, 252 (2013).
[23] M. Aykol and C. Wolverton, Phys. Rev. B **90**, 115105 (2014).
[24] C. Wolverton and K. C. Hass, Phys. Rev. B **63**, 024102 (2000).
[25] S. C. Parker, P. M. Oliver, N. H. De Leeuw, J. O. Titiloye, and G. W. Watson, Phase Transitions **61**, 83 (1997).
[26] G. Kresse and J. Hafner, Phys. Rev. B **47**, 558 (1993).
[27] G. Kresse and J. Furthmüller, Comput. Mater. Sci. **6**, 15 (1996).
[28] G. Kresse and D. Joubert, Phys. Rev. B **59**, 1758 (1999).
[29] S. L. Dudarev, G. A. Botton, S. Y. Savrasov, C. J. Humphreys, and A. P. Sutton, Phys. Rev. B **57**, 1505 (1998).
[30] J. E. Saal, S. Kirklin, M. Aykol, B. Meredig, and C. Wolverton, JOM **65**, 1501 (2013).
[31] A. R. Akbarzadeh, V. Ozoliņš, and C. Wolverton, Adv. Mater. **19**, 3233 (2007).
[32] P. W. Tasker, J. Phys. C: Solid State Phys. **12**, 4977 (1979).
[33] D. Kramer and G. Ceder, Chem. Mater. **21**, 3799 (2009).
[34] A. Jain, G. Hautier, S. P. Ong, C. J. Moore, C. C. Fischer, K. A. Persson, and G. Ceder, Phys. Rev. B **84**, 045115 (2011).
[35] M. W. Chase, C. A. Davies, J. R. Downey, D. J. Frurip, R. A. McDonald, and A. N. Syverud, J. Phys. Chem. Ref. Data, Suppl. **14**, 1 (1985).
[36] R. V. Zucker, D. Chatain, U. Dahmen, S. Hagège, and W. C. Carter. J. Mater. Sci. **47**, 8290 (2012).
[37] K. Momma and F. Izumi, J. Appl. Crystallogr. **44**, 1272 (2011).
[38] C. Y. Ouyang, S. Q. Shi, and M. S. Lei, J. Alloys Compd. **474**, 370 (2009).
[39] D. Vanderbilt, Phys. Rev. B **41**, 7892 (1990).
[40] Y. Wang and J. P. Perdew, Phys. Rev. B **44**, 13298 (1991).
[41] D. Tang, Y. Sun, Z. Yang, L. Ben, L. Gu, and X. Huang, Chem. Mater. **26**, 3535 (2014).
[42] Y.-K. Sun and S.-H. Jin, J. Mater. Chem. **8**, 2399 (1998).
[43] Y.-S. Lee, Y.-K. Sun, and K.-S. Nahm, Solid State Ionics **109**, 285 (1998).
[44] M. Takahashi, T. Yoshida, A. Ichikawa, K. Kitoh, H. Katsukawa, Q. Zhang, and M. Yoshio, Electrochim. Acta **51**, 5508 (2006).
[45] W. Liu, K. Kowal, and G. C. Farrington, J. Electrochem. Soc. **143**, 3590 (1996).
[46] Y. Gao and J. R. Dahn, J. Electrochem. Soc. **143**, 1783 (1996).